







RESEARCH ARTICLE | MARCH 22 2024

Improving the mechanical properties of Cantor-like alloys with Bayesian optimization

Valtteri Torsti ; Tero Mäkinen  ; Silvia Bonfanti ; Juha Koivisto ; Mikko J. Alava 



APL Mach. Learn. 2, 016119 (2024)

<https://doi.org/10.1063/5.0179844>



30 July 2024 12:56:26



APL Energy

Latest Articles Online!

Read Now



Improving the mechanical properties of Cantor-like alloys with Bayesian optimization

Cite as: APL Mach. Learn. 2, 016119 (2024); doi: 10.1063/5.0179844

Submitted: 5 October 2023 • Accepted: 5 March 2024 •

Published Online: 22 March 2024



Valtteri Torsti,¹ Tero Mäkinen,^{1,a)} Silvia Bonfanti,² Juha Koivisto,¹ and Mikko J. Alava^{1,2}

AFFILIATIONS

¹ Department of Applied Physics, Aalto University, PO Box 11000, 00076 AALTO Espoo, Finland

² NOMATEN Centre of Excellence, National Center for Nuclear Research, ul. A. Soltana 7, 05-400 Swierk/Otwock, Poland

^{a)} Author to whom correspondence should be addressed: tero.j.makinen@aalto.fi

ABSTRACT

The search for better compositions in high entropy alloys is a formidable challenge in materials science. Here, we demonstrate a systematic Bayesian optimization method to enhance the mechanical properties of the paradigmatic five-element Cantor alloy *in silico*. This method utilizes an automated loop with an online database, a Bayesian optimization algorithm, thermodynamic modeling, and molecular dynamics simulations. Starting from the equiatomic Cantor composition, our approach optimizes the relative fractions of its constituent elements, searching for better compositions while maintaining the thermodynamic phase stability. With 24 steps, we find Fe₂₁Cr₂₀Mn₅Co₂₀Ni₃₄ with a yield stress improvement of 58%, and with 72 steps, we find Fe₆Cr₂₂Mn₅Co₃₂Ni₃₅ where the yield stress has improved by 74%. These optimized compositions correspond to Ni-rich medium entropy alloys with enhanced mechanical properties and superior face-centered-cubic phase stability compared to the traditional equiatomic Cantor alloy. The automatic approach devised here paves the way for designing high entropy alloys with tailored properties, opening avenues for numerous potential applications.

© 2024 Author(s). All article content, except where otherwise noted, is licensed under a Creative Commons Attribution (CC BY) license (<http://creativecommons.org/licenses/by/4.0/>). <https://doi.org/10.1063/5.0179844>

I. INTRODUCTION

Metallic alloying has historically been the key factor in opening up new possibilities for designing materials with desired properties. The advent of the new class of high entropy alloys (HEAs),^{1,2} or multi-principal element alloys (MPEAs), represented a paradigm shift in alloy design strategies. Unlike conventional alloys, which are typically made up by one or two major atomic species, HEAs are distinguished by the presence of several metallic species, five or more, in nearly equal concentration. Mixing many elements might alter their interaction, providing a chance to get exceptional mechanical properties, e.g., improved hardness and a higher degree of fracture resistance.³ Consequently, a key factor that emerged in HEAs is the richness in *composition*, which brings additional degrees of freedom in terms of atomic species, e.g., Mn, Cr, Fe, Co, Ni, and Cu. A crystalline material, like conventional alloys, has a periodically ordered structure in terms of positional degrees of freedom. Meanwhile, a crystalline HEA maintains an ordered structure in position but shows a disordered pattern in terms of compositional degrees of freedom (*compositional disorder*): the atomic

species are randomly distributed on the lattice sites. Our understanding of the effect of the microscopic compositional disorder on the mechanical properties of HEAs^{4–7} is limited to the applications of classical mean-field like ideas of dislocation depinning. The microscopic origin of their failure mechanisms also remains elusive, particularly because in experiments it is challenging to probe such scales.

Gaining insights into the microscopic structure and its relation to mechanical properties would lead to new design principles for desired HEAs. However, due to the huge degree of freedom in terms of composition, finding HEAs with optimal desired properties is also challenging. Given the aleatory nature of HEAs, the landscape of mechanical properties in the compositional space is expected to be rugged.

The compositional search problem can be tackled by extensive experimentation,^{8–12} but machine learning methods^{13–21} as well as computational approaches^{22–25} are needed for rapid exploration of the search space. Classical molecular dynamics (MD) is a method that allows for the computational probing of the mechanical properties of different alloy compositions. While still restricted to fairly

small system sizes, these can be significantly larger than those used with *ab initio* methods.

Here, to probe the high-dimensional search space even more efficiently, we employ active learning methods.^{26–30} These methods aim to identify optimal compositions with a minimal computational cost. We use Bayesian optimization (BO) to initially explore the search space and then to exploit the gathered information in finding the optimal composition. We study *in silico* the equiatomic Cantor alloy (FeCrMnCoNi)¹ as the paradigmatic HEA and vary its composition around the equiatomic starting point. A practical reason for this is, in addition to the large interest in this system, the availability of MD potentials.

The phase stability of HEAs is a critical factor that influences the alloy's properties and performance. The Cantor alloy is known to have a face-centered cubic (fcc) lattice structure at high temperatures, and if we want to maintain this property, we have to impose constraints on the available search space. The general benefit of having an fcc structure is the increased ductility due to the increased density of slip systems. There are many ways of determining the lattice structure of a specific composition, such as experimental investigations,^{9,10,12,31} estimation based on modified Hume-Rothery rules³² (see Appendix B), or density functional theory (DFT) calculations,³³ but here we have opted to do it using the computationally low-cost calculation of phase diagrams (CALPHAD)³⁴ method. This method uses a thermodynamic database to compute, for example, the phase fraction of fcc for the given composition and temperature, and this information can be used to constrain the optimization to only fcc lattices.

In this work, we introduce for the first time an automated protocol (see Fig. 1), which combines an online database, a Bayesian

optimization algorithm for the selection of the subsequent composition, thermodynamic modeling to ensure fcc phase stability, and molecular dynamics simulations to probe the mechanical properties. Our goal is to search for Cantor-like HEAs with optimal mechanical properties. In the following, we start by exploring the effect of the fcc constraint on the search space, then describe the search process, and finally describe the optimized Cantor-like HEAs.

II. METHODS

The main method we use is BO,^{30,35–37} where the mechanical properties at each point in the compositional space are represented by a probabilistic surrogate function, which is constructed based on currently known input data and is typically a Gaussian process regressor. This probabilistic representation can then be used for further measurements based on the chosen utility function: one can focus on exploration by examining points where the uncertainty in the probabilistic representation is high, or on exploitation by focusing on points where the value of the mechanical property of interest is expected to be high. Gaussian process regressors require far fewer hyperparameters to be fitted compared, for example, to neural networks, and this translates to significantly smaller datasets needed during BO.

We take as the input the point in the composition space (search space) $\mathbf{x} = [c_{\text{Fe}}, c_{\text{Cr}}, c_{\text{Mn}}, c_{\text{Co}}, c_{\text{Ni}}]$, which is just a vector of the atomic composition c_i of the Cantor-like alloy. As the constraint $\sum_i c_i = 1$ sets up a 4-dimensional manifold in the 5D space, we can simply do the optimization in the 4D space given by the first 4 compositions. The output used here is the yield stress τ_y , but one could just as well optimize for any other mechanical property.

We use Gaussian Process Regression (GPR),³⁸ implemented in the scikit-learn software,³⁹ where the desired quantity y for each point \mathbf{x} in the search space is represented by a Gaussian distribution with mean $\mu(\mathbf{x})$ and standard deviation $\sigma(\mathbf{x})$. The kernel used in the GPR is based on the anisotropic radial basis function,

$$k_{\text{RBF}}[y(\mathbf{x}), y(\mathbf{x}')] = k_0^2 \exp \left(- \sum_{i=1}^{N-1} \frac{(x_i - x'_i)^2}{2\ell_i^2} \right), \quad (1)$$

where x_i is the i th component of \mathbf{x} and ℓ_i is a length scale related to the i th component. To account for the variation in the yield stress due to the specific atomic configuration, a white noise kernel, $k_{\text{WN}}[y(\mathbf{x}), y(\mathbf{x}')] = w^2 \delta(|\mathbf{x} - \mathbf{x}'|)$, where δ is the Dirac delta function and the norm is the Euclidean distance, is added. The total kernel is then given by the covariance $\text{cov}[y(\mathbf{x}), y(\mathbf{x}')] = k_{\text{RBF}} + k_{\text{WN}}$. The kernel hyperparameters w , k_0 , and ℓ_i optimized in the GPR algorithm are chosen to have the following initial values: w is initially the standard deviation of the yield stress in the current dataset $\Delta\tau_y$, k_0 is four times this value, and the length scales ℓ_i are bounded by the minimum and maximum spacing of the data points in the dataset⁴⁰ (i.e., the minimum and maximum differences of c_i in the dataset) and initialized to the mean of these two values. The evolution of the hyperparameters during the search is discussed in Appendix A.

The optimization starts from the equiatomic Cantor alloy, and the next two points are picked from the neighboring grid points to ensure fcc stability. After this, the next point is picked based

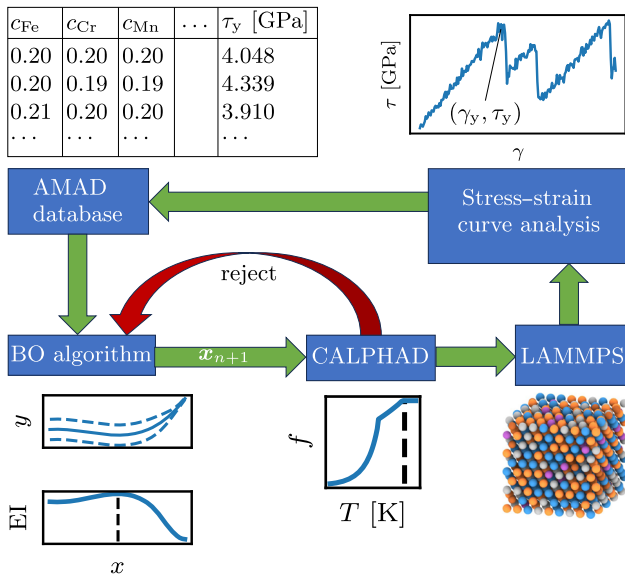


FIG. 1. Workflow of the optimization process, including an online database for data storage, a Bayesian optimization algorithm determining the next best point in the composition space \mathbf{x}_{n+1} , a thermodynamic analysis of the composition to constrain the alloy to fcc lattice structure, and finally a molecular dynamics simulation and the associated analysis of the stress-strain curves.

on the highest value of the utility function. We have here chosen as the utility function the expected improvement, which is defined as $EI(\mathbf{x}) = \int_{y^*}^{\infty} (y - y^*) \mathcal{N}_{\mu(\mathbf{x}), \sigma(\mathbf{x})}(y) dy$, where y^* is the current highest value of the desired quantity and $\mathcal{N}_{\mu, \sigma}$ is the probability density function of the Gaussian distribution with mean μ and standard deviation σ .

This type of optimization in a grid can quite rapidly run into the situation where the maximal expected improvement is achieved at a point already previously visited. There are multiple choices one can make here: one can consider the optimization converged, pick a random point from the search space,⁴¹ or pick the point in the grid with the next highest expected improvement, which is what we have done here. Here, we consider the optimization to have converged, when the expected improvement normalized by the current best value reaches a value less than 10^{-3} . This point is fairly arbitrary and other thresholds could be set.

To restrict the search to only fcc alloys, we perform CALPHAD calculations using the PyCalphad⁴² software and the associated MPEA database. In the CALPHAD method, thermodynamic calculations are performed based on a thermodynamic database. By minimizing the Gibbs free energy, one can find the phase with the lowest free energy under a given set of conditions. Using this method, we compute the fcc phase fraction f at the desired temperature and atmospheric pressure for each composition in the search space. This can be done for each of the points as they are given by the BO algorithm, but as our search grid is sufficiently small, we have precomputed all the values and find them from a lookup table. To test the accuracy of our CALPHAD calculations, we did the same calculations with the FactSage software⁴³ and the FSstel database for a few compositions (the compositions of iterations 1, 24, 50, and 74). In the region where $0 < f < 1$ based on FactSage, PyCalphad on average overestimates f by 19%. However, at 900 K, $f = 1$ for all the compositions, except for $\text{Fe}_5\text{Cr}_{30}\text{Mn}_5\text{Co}_{25}\text{Ni}_{35}$ (iteration 50, $f = 0.91$), which becomes fully fcc only at 985 K.

To test the mechanical properties of each composition, we perform MD simulations using LAMMPS.⁴⁴ These are shear simulations performed in three dimensions with periodic boundary conditions. The interaction between the atoms is given by the modified embedded atom method (MEAM) interatomic potential and using the Cantor HEA parameters.⁴⁵ It is acknowledged that MEAM tends to overestimate the yielding point in several Cantor family alloys, but its value in conducting composition searches for alloys with improved mechanical properties remains significant. MD simulations using MEAM consistently align with experimental results, reflecting a comparative trend in yield stress across various Cantor-like alloy compositions,⁴⁵ and are known to predict well thermal properties such as melting points for several Cantor family alloys, as demonstrated in Ref. 46.

The system starts with all atoms initialized in an fcc nickel crystal structure, with the [110] direction aligning with the x -axis, the $[-111]$ direction aligning with the y -axis, and the $[1-12]$ direction aligning with the z -axis. Atoms are then substituted according to the proportions provided by the BO algorithm (i.e., \mathbf{x}_{n+1}), with atomic species being Ni, Co, Cr, Fe, and Mn. The simulation box is then incrementally sheared along the x -direction with respect to the y -direction by δy , which is 0.1%, and at each strain increment, MD simulations are performed for a duration of 1 ps. Throughout the shearing process, we record the stress-strain response, which

provides a detailed stress-strain curve for analysis. The MD simulations are conducted at 900 K.

The system size used here is 1080 atoms, and the effects on increasing system size are discussed in Appendix C. The mechanical property we focus on is the yield stress τ_y , which is determined as the maximal shear stress τ achieved before a stress drop of at least 1 GPa. In addition, the shear modulus, determined as the ratio between the yield stress and yield strain, $G = \tau_y/\gamma_y$, is recorded. For each composition, 100 realizations of the atomic configurations are simulated and the mean values (and the standard deviations) of the yield stress and shear modulus are used. Note that one could naturally compute the mechanical response in all the main crystallographic directions and, for example, average the yield stress over these.

The workflow (illustrated in Fig. 1) starts with a database stored in the Aalto Materials Digitalization Platform (AMAD), which has an initial set of inputs (for the first step, the composition of the equiatomic Cantor alloy $c = 0.2$) and outputs. The database is read automatically by the BO algorithm, which performs GPR in a grid with a concentration step $\Delta c = 0.01$ and boundaries $0.05 \leq c \leq 0.35$, which is the window in which we let the concentrations to vary around the equiatomic starting point. The algorithm outputs a list of points that correspond to the highest values of the utility function. The result of the CALPHAD computation is checked for each of these points, until a point with a sufficiently high fcc phase fraction (here $f = 1$) is found. The composition corresponding to this point is given as an input to the shear simulation, and after the yield stress is determined, the composition and the corresponding yield stress are written back to the AMAD database. This process is automatically iterated, until the algorithm has converged to an optimal composition.

Here, the role of the AMAD database is just to store a table of values. It provides easy interfacing with the data from the computational cluster running the simulations, as well as for humans interacting with the data via a web interface.

As the time required to perform a single CALPHAD computation (less than 1 s) is small, it can be done for the whole search grid of 553 401 points in 154 CPU hours. Meanwhile, with 16 CPUs, each LAMMPS simulation takes around 7 min and performing these in parallel means that each iteration takes roughly 7 min. This then means that 24 iterations can be performed in around 3 h and 80 iterations in around 9 h, with the number of CPU hours being 4480 and 14 933, due to the 100 realizations for each run.

III. RESULTS

A. Mapping and exploration of the composition space

The effect of the fcc lattice structure constraint changes with temperature. As our search grid is small enough, we can precompute the fcc phase fraction of each composition at different temperatures and see exactly how the fcc constraint limits the search space. The cumulative distributions of phase fractions are shown in Fig. 2, and one can see that, for example, at 700 K, less than 20% of the search space has a single phase fcc structure, whereas at 1100 K, this is true for almost 80% of the search space.

From Fig. 2, one can also see that based on CALPHAD calculations, our starting point—the equiatomic Cantor alloy—itself only has a single phase fcc structure at temperatures above ~ 900 K.³¹

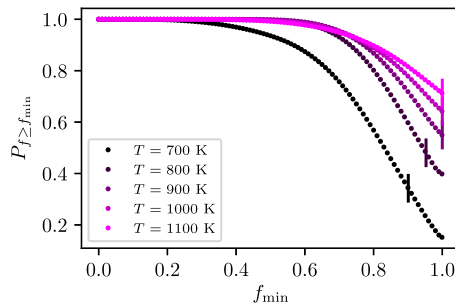


FIG. 2. Cumulative probability density function of the fcc phase fraction (considering all the compositions in our grid) for a few temperatures. The vertical line indicates the fcc phase fraction of the equiatomic Cantor alloy.

Therefore, we have chosen to perform our optimization at this temperature, as it provides the most interesting constrained optimization problem while maintaining the desired structure for the starting point alloy.

B. Search process

Starting from the equiatomic Cantor alloy and picking the next two initial points from its immediate neighborhood means that the yield stress does not change much in this initial stage. As can be seen from Fig. 3, during the subsequent BO steps, the composition does not change significantly [panel (c)] and the best yield stress does not change (the black solid line in [panel (a)]). After the first 16 iterations, BO starts rapidly replacing Mn with Ni and, in just

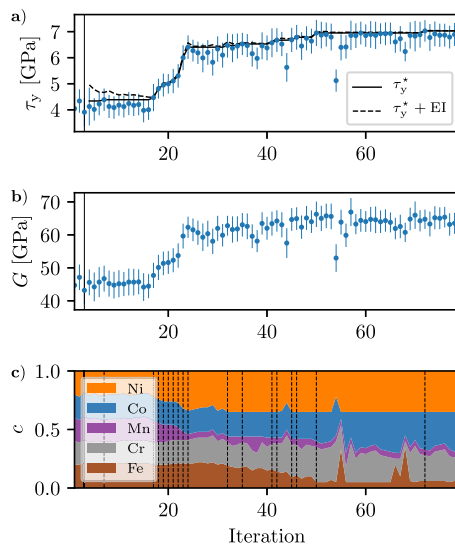


FIG. 3. Evolution of (a) the yield stress τ_y and (b) the shear modulus G as a function of the iteration number, as well as (c) the composition used for each iteration. The black solid line in panel (a) represents the current best yield stress value τ_y^* , and the black dashed line represents the expected improvement over this current best value. The solid vertical line indicates the beginning of the BO process, and the dashed vertical lines in panel (c) indicate the iterations where a new current best value of the yield stress was achieved.

eight iterations, achieves an improvement of 58% compared to the starting point. After this point, the BO algorithm keeps exploring (mostly by decreasing c_{Fe}) and, at 50 iterations, has achieved an improvement of additional 13% points. The final best composition $Fe_6Cr_{22}Mn_5Co_{32}Ni_{35}$, before we consider the algorithm to have converged, is achieved at iteration 72 where the total improvement compared to the starting point is 74%. The algorithm converges at 80 iterations. See Appendix B for additional details on the evolution of different parameters during the search and Appendix D for the goodness-of-fit analysis.

The evolution of the shear modulus G can also be seen in panel (b) of Fig. 3. It roughly follows the same trend as the yield stress, so the optimization is not optimizing for yield stress by finding some strong but brittle alloys, but rather concomitantly optimizing for yield stress and yield strain. The highest shear modulus $G = 66.9 \pm 4.2$ GPa is found at iteration 57 and corresponds to a 50% improvement over the initial value.

C. Optimized fcc Cantor-like HEA

The average stress-strain curves of certain iterations can be seen in Fig. 4. As explained in Sec. III B, most of the improvement has already been made by iteration 24, when the algorithm has moved to the Ni-rich part of the search space. After that (iterations 50 and 72 shown), the improvements are much more minor. The last three iterations shown are characterized by high Ni concentrations and low Mn and Fe concentrations, effectively converging to a NiCoCr medium entropy alloy. One realization of the alloy corresponding to iteration 72 can be seen in the top left corner of Fig. 4.

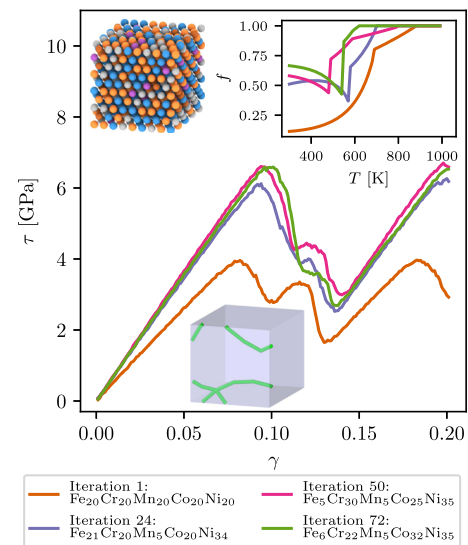


FIG. 4. Stress-strain curves for the initial equiatomic Cantor alloy (iteration 1) and for three iterations that had the optimal yield stress up to that point in the optimization. The inset shows the fcc phase fraction f , computed using CALPHAD, as a function of temperature T for the same iterations. The top left corner shows one realization of the composition corresponding to iteration 72 [colors as in Fig. 3(c)], and in the bottom, the dislocation loop formed in the sample during yielding at the stress peak is shown.

Very similar results are obtained with larger, more realistic, system sizes (see Appendix C). One can also see that the improvement in yield stress also corresponds to an improvement in the yield strain. The peak in the stress–strain curve is accompanied by the appearance of dislocations (bottom, Fig. 4), with the resulting flow being accompanied by a decrease in the stress beyond the peak. In the inset of Fig. 4, the fcc phase fraction f is plotted as a function of the temperature T for each of the compositions shown in the main figure. As explained earlier, the chosen $T = 900$ K is very close to the value where the fcc phase fraction of equiatomic Cantor starts to dip below unity as the temperature is decreased. However, all three of the optimized compositions have higher fcc phase stability, the final one (iteration 72) having a single phase fcc structure at temperatures above around 600 K.

IV. DISCUSSION

We have implemented an automated system for exploring the compositional space of Cantor-like HEAs, under the constraint of a single phase fcc structure. This is done by utilizing Bayesian optimization, CALPHAD calculations of the fcc phase fractions, and molecular dynamics shear simulations.

The optimization starts from the equiatomic FeCrMnCoNi alloy and, in 72 iterations, moves to Fe₆Cr₂₂Mn₅Co₃₂Ni₃₅, which is effectively a NiCoCr⁴⁷ medium entropy alloy (MEA). The improvement in the yield stress is 74%. Already at iteration 24, a yield stress improvement of 58% is found with Fe₂₁Cr₂₀Mn₅Co₂₀Ni₃₄. Both of these compositions have higher fcc phase stability than the equiatomic Cantor alloy. The preference to high-Ni alloys is not exactly a surprise,^{45,47–49} and in the realm of low entropy alloys, Ni-based superalloys⁵⁰ are commonly used in high-temperature applications.

From the viewpoint of advanced Bayesian applications, there are two issues at hand we should mention. The first one is the feasibility of solutions issue. In our case, this turns out to be of secondary importance since the pruning of many candidate compositions due to not filling the constraint (fcc fraction in our case) is not a major challenge. If the solution space would be much more restricted—even in similar cases as ours (optimizing alloy compositions *in silico* with one or more material parameters to be optimized)—exploiting information to concentrate the search in more optimal phase space regions is the way to go. Our case is a typical example in that the constraint of the optimization is a binary variable, also adaptable to Bayesian approaches, and in such cases, one would often like to know the boundaries of the feasible region, a hard task.^{27,28,51–53}

Multiobjective optimization was not needed nor tried here, as optimizing for yield stress in our system does not seem to result in strength–ductility trade-offs. Instead, both are concomitantly increased, a feature more commonly seen in hierarchical systems.^{54–56} Nevertheless, more complex (compositional) search landscapes would make this both interesting and necessary. Recent work in the materials design with multiple criteria in mind basically splits into two approaches. Either one works out an *ad hoc* scalar cost function combining the criteria by a set of weights, or searches for the full Pareto optimal front. As this is a phase space region identification task, it is like the feasibility space one by necessity a harder effort.⁵³

In specific practical applications, some atomic species might have very specific uses,⁵⁷ which we have not considered here. We have only considered mechanical properties, ignoring, for example, thermal conductivity properties. In addition, we have here focused on a simple random fcc structure. To make the systems more realistic, one might also explore the effects of short-range ordering,⁵⁸ for example, using swap Monte Carlo methods.⁵⁹ This would present another dimension to the search problem via the tendency of short-range order. One should also experimentally verify the mechanical properties of the optimal HEAs established here. We have also not considered the temperature dependence of the optimal compositions⁶⁰ here, but just focused on a single temperature of 900 K. Another multiobjective task would naturally be to optimize the composition in a range of temperatures of interest.

Due to the modular structure of the automated system, further work using different potentials^{61–63} for systems differing from the Cantor-like HEAs would not require major changes to the framework. In addition, changing the utility function to optimize for something completely different, e.g., the yield stress per price of the material, is a simple task in the framework. Even replacing the whole molecular dynamics part with, for example, experimental results is easy, although the time for each iteration step increases significantly. Our focus here is in showing a workflow for composition optimization, not one for automated experiments.

ACKNOWLEDGMENTS

We thank Daniel Lindberg for the computation of CALPHAD results using FactSage. S.B. and M.J.A. are supported by the European Union Horizon 2020 research and innovation program under Grant Agreement No. 857470 and the European Regional Development Fund via the Foundation for Polish Science International Research Agenda PLUS program under Grant No. MAB PLUS/2018/8. M.J.A. acknowledges the support from the Academy of Finland (Center of Excellence program, Grant Nos. 278367 and 317464). T.M., J.K., and M.J.A. acknowledge the support from the FinnCERES flagship (Grant No. 151830423), Business Finland (Grant Nos. 211835 and 211909), and Future Makers programs. J.K. acknowledges funding from the Academy of Finland (Grant No. 308235) and Business Finland (Grant No. 211715). The authors acknowledge the computational resources provided by the Aalto University School of Science “Science-IT” project.

AUTHOR DECLARATIONS

Conflict of Interest

The authors have no conflicts to disclose.

Author Contributions

Valtteri Torsti: Data Curation (equal); Formal Analysis (equal); Investigation (equal); Methodology (equal); Software (lead); Visualization (equal); Writing – Review & Editing (equal). **Tero Mäkinen:** Conceptualization (equal); Data Curation (equal); Formal Analysis (equal); Funding Acquisition (equal); Investigation (equal); Methodology (equal); Software (equal); Supervision (equal); Visualization (equal); Writing – Original Draft Preparation (lead);

Writing – Review & Editing (equal). **Silvia Bonfanti**: Conceptualization (lead); Data Curation (equal); Methodology (equal); Software (equal); Supervision (equal); Project Administration (lead); Visualization (equal); Writing – Original Draft Preparation (equal); Writing – Review & Editing (equal). **Juha Koivisto**: Conceptualization (equal); Funding Acquisition (equal); Methodology (equal); Project Administration (equal); Supervision (equal); Writing – Review & Editing (equal). **Mikko Alava**: Conceptualization (lead); Funding Acquisition (lead); Methodology (equal); Project Administration (lead); Supervision (equal); Writing – Original Draft Preparation (lead); Writing – Review & Editing (equal).

DATA AVAILABILITY

The data that support the findings will be available at <https://doi.org/10.5281/zenodo.10535904> following an embargo from the date of publication until July 1, 2024, to allow for the commercialization of research findings.

APPENDIX A: EVOLUTION OF KERNEL HYPERPARAMETERS

The hyperparameters of the BO algorithm, w , k_0 , and ℓ_i , are optimized during each iteration. This allows us to see how they evolve with the increasing dataset size (see Fig. 5). Initially, the white noise w [panel (a)] in the system is zero and k_0 [panel (b)] decreases with increasing dataset size. This means that the BO algorithm thinks that the correlation between the yield stress values between points close to each other in the composition space is low, i.e., the landscape is rugged. However, when areas further from the equiatomic composition are explored around iteration 20, w and k_0 increase, meaning that the BO algorithm considers this correlation to be higher and the ruggedness of the yield stress landscape to be just modeled with a white noise type error term. It is noteworthy that even the highest values of w are significantly lower than the

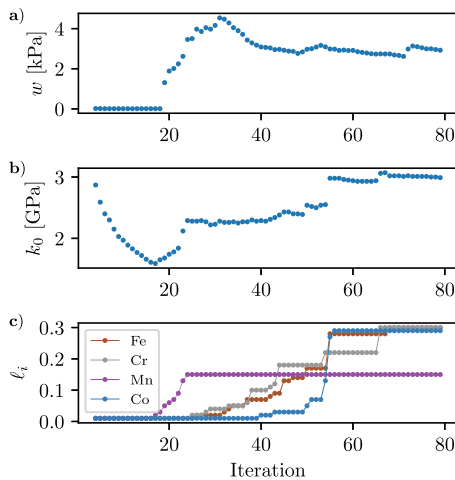


FIG. 5. Evolution of the hyperparameters corresponding to the (a) prefactor of the white noise kernel, (b) prefactor of the RBF kernel, and (c) length scales of the RBF kernel, as a function of the iteration number.

actual variation in the yield stress due to different realizations of the same composition $\Delta\tau_y = 467 \pm 55$ kPa. The standard deviation $\sigma(\mathbf{x})$ is then mostly given by the RBF kernel—i.e., k_0 , which has values significantly higher than $\Delta\tau_y$.

Initially, the step sizes of the algorithm are small, so all the length scales ℓ_i are bounded close to the $\Delta c = 0.01$ value. Around the same iteration 20 point, they start to increase, once again indicating that the yield stress landscape is not very rugged after all. The length scale values keep increasing close to the maximum values (maximum distance of points in the dataset). The kernel is then fairly isotropic, the smallest length scale being ℓ_{Mn} . This is simply due to the observation that the optimal HEAs are found with very low values of c_{Mn} , so higher values are not explored.

APPENDIX B: EVOLUTION OF ADDITIONAL QUANTITIES

There is a plethora of quantities one can compute based on the compositions and the results of the MD simulations. Some of these are shown in Fig. 6. The vertical lines in this figure indicate the iterations where a current optimal composition (in terms of yield stress) has been found.

The expected improvement EI is shown already in Fig. 3, but the evolution is more clear in logarithmic scale [Fig. 6(a)]. The expected improvement normalized by the current best yield stress EI/τ_y [Fig. 6(b)] shows how the optimization moves toward the convergence criterion $\text{EI}/\tau_y \leq 10^{-3}$ and how a different threshold would change the number of iterations performed by the algorithm.

Another illustration of the search done by the algorithm is the Euclidean distance from the equiatomic Cantor alloy $|\mathbf{x} - \mathbf{x}_C|$, shown in Fig. 6(c). One can see that the algorithm stays close to the equiatomic composition and, until around iteration 20, starts to rapidly move away from it. The distance increases, and, until around iteration 50, it settles into a roughly constant value. This is simply due to the fact that the compositions explored are at the edge of the search space.

In this work, we have defined the search space by one definition of HEAs: all the concentrations being between 5% and 35%.² One could also define HEAs as alloys having mixing entropy $S_{\text{mix}} = -R \sum_i c_i \ln c_i > 1.5R$,⁶⁴ where R is the molar gas constant. The MEAs would then be defined as alloys with mixing entropies $R \leq S_{\text{mix}} \leq 1.5R$. The evolution of the mixing entropy S_{mix}/R is shown in Fig. 6(d). During optimization, the mixing entropy of our alloys decreases to roughly 1.4, putting them into the MEA category. However, at iteration 24, we are still very close to $S_{\text{mix}} = 1.5R$.

One of the quantities often computed for HEAs is the lattice distortion parameter,⁶⁵

$$\delta = \sqrt{\sum_{i=1}^N c_i \left(1 - \frac{r_i}{\sum_{i=1}^N c_i r_i}\right)^2}, \quad (\text{B1})$$

where c_i are the atomic compositions ($N = 5$) and r_i is the corresponding atomic radii. One of the modified Hume-Rothery rules is that small lattice distortion favors single-phase formation. For the atomic radii,⁶⁶ one can take the Goldschmidt radius of each atomic species [Fig. 6(e)] or the effective radius based on a more realistic configuration [Fig. 6(f)]. On average, we can see that the δ parameter

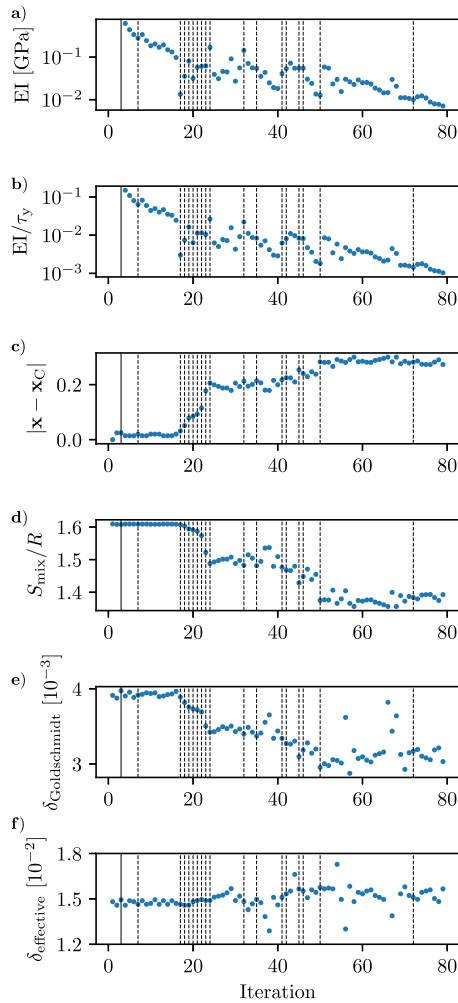


FIG. 6. Evolution of additional parameters: (a) expected improvement, (b) expected improvement normalized by the current best yield stress, (c) Euclidean distance from the equiatomic Cantor alloy in the compositional space, (d) the mixing entropy (normalized by the molar gas constant), (e) the δ parameter [Eq. (B1)] computed using the Goldschmidt radii, and (f) the δ parameter computed using the effective radii, as a function of the number of iterations.

computed based on the Goldschmidt radii $\delta_{\text{Goldschmidt}}$ decreases with the iterations (i.e., with increasing yield stress), but the one computed based on the effective radii $\delta_{\text{effective}}$ slightly increases with the iterations.

APPENDIX C: EFFECT OF THE SYSTEM SIZE

The stress-strain curves corresponding to the system size of 1080 atoms for four compositions are shown in Fig. 4. The stress-strain curves for the same compositions but with system sizes of 9504 [panel (a)] and 93 840 [panel (b)] atoms are shown in Fig. 7.

The greatest distinction from the smaller systems is that $\text{Fe}_{21}\text{Cr}_{20}\text{Mn}_5\text{Co}_{20}\text{Ni}_{34}$ performs better than $\text{Fe}_5\text{Cr}_{30}\text{Mn}_5\text{Co}_{35}\text{Ni}_{25}$.

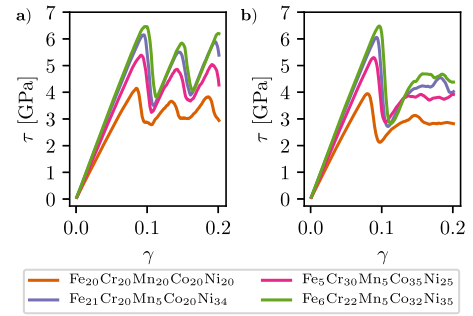


FIG. 7. Stress-strain curves corresponding to the systems illustrated in Fig. 4, but for system sizes of (a) 9504 and (b) 93 840 atoms.

The results in terms of yield stress for the equiatomic Cantor and the best alloy with smaller systems, $\text{Fe}_6\text{Cr}_{22}\text{Mn}_5\text{Co}_{32}\text{Ni}_{35}$, are basically the same with all system sizes.

In the smallest systems, one can see a large stress drop lasting around 5% in strain and then a stress increase, but in the systems with 9504 atoms, the stress drops are quicker and there are several of them. Finally, in the largest systems, there is a single large stress drop, and after that, the stress-strain curves look roughly horizontal implying continuous flow.

APPENDIX D: GOODNESS-OF-FIT

Even using a simple radial basis function kernel, the predictions given by GPR align well with the observed data, as illustrated in Fig. 8. In the early stages of the optimization [for example, at iteration 28 shown in Fig. 8(a)], the GPR fits the training data well, but the yield stress at the next simulation point might be strongly underestimated by the GPR, although the GPR does give wide error margins for the estimate. During the final iterations (around iteration 60 onward), the yield stress starts to be well predicted by the GPR, as can be seen from Fig. 8(b). This is consistent with the behavior seen in Fig. 3(a).

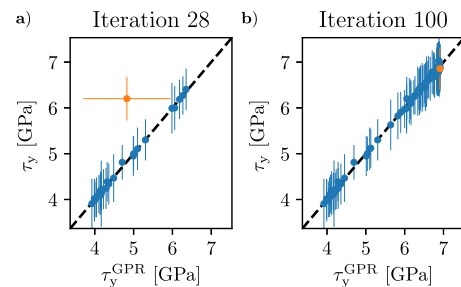


FIG. 8. Yield stress obtained from the simulations τ_y vs the yield stress predicted by GPR τ_y^{GPR} at (a) iteration 28 and (b) iteration 100. The blue points correspond to the training data, and the orange points correspond to the newest point (test data).

REFERENCES

- ¹ B. Cantor, I. Chang, P. Knight, and A. Vincent, "Microstructural development in equiatomic multicomponent alloys," *Mater. Sci. Eng.: A* **375–377**, 213–218 (2004).
- ² J.-W. Yeh, S.-K. Chen, S.-J. Lin, J.-Y. Gan, T.-S. Chin, T.-T. Shun, C.-H. Tsau, and S.-Y. Chang, "Nanostructured high-entropy alloys with multiple principal elements: Novel alloy design concepts and outcomes," *Adv. Eng. Mater.* **6**, 299–303 (2004).
- ³ E. P. George, D. Raabe, and R. O. Ritchie, "High-entropy alloys," *Nat. Rev. Mater.* **4**, 515–534 (2019).
- ⁴ C. Varvenne, A. Luque, and W. A. Curtin, "Theory of strengthening in fcc high entropy alloys," *Acta Mater.* **118**, 164–176 (2016).
- ⁵ Z. Li and D. Raabe, "Strong and ductile non-equiatomic high-entropy alloys: Design, processing, microstructure, and mechanical properties," *JOM* **69**, 2099–2106 (2017).
- ⁶ G. Laplanche, J. Bonneville, C. Varvenne, W. Curtin, and E. George, "Thermal activation parameters of plastic flow reveal deformation mechanisms in the CrMnFeCoNi high-entropy alloy," *Acta Mater.* **143**, 257–264 (2018).
- ⁷ G. Bracq, M. Laurent-Brocq, C. Varvenne, L. Perrière, W. Curtin, J.-M. Joubert, and I. Guillot, "Combining experiments and modeling to explore the solid solution strengthening of high and medium entropy alloys," *Acta Mater.* **177**, 266–279 (2019).
- ⁸ Y. Liu, Y. Zhang, H. Zhang, N. Wang, X. Chen, H. Zhang, and Y. Li, "Microstructure and mechanical properties of refractory HfMo_{0.5}NbTiV_{0.5}Si_x high-entropy composites," *J. Alloys Compd.* **694**, 869–876 (2017).
- ⁹ J. E. Saal, I. S. Berglund, J. T. Sebastian, P. K. Liaw, and G. B. Olson, "Equilibrium high entropy alloy phase stability from experiments and thermodynamic modeling," *Scr. Mater.* **146**, 5–8 (2018).
- ¹⁰ G. Qin, W. Xue, C. Fan, R. Chen, L. Wang, Y. Su, H. Ding, and J. Guo, "Effect of Co content on phase formation and mechanical properties of (AlCoCrFeNi)_{100-x}Co_x high-entropy alloys," *Mater. Sci. Eng.: A* **710**, 200–205 (2018).
- ¹¹ Q. Ding, Y. Zhang, X. Chen, X. Fu, D. Chen, S. Chen, L. Gu, F. Wei, H. Bei, Y. Gao, M. Wen, J. Li, Z. Zhang, T. Zhu, R. O. Ritchie, and Q. Yu, "Tuning element distribution, structure and properties by composition in high-entropy alloys," *Nature* **574**, 223–227 (2019).
- ¹² C. Wagner, A. Ferrari, J. Schreuer, J.-P. Couzinié, Y. Ikeda, F. Körmann, G. Eggeler, E. P. George, and G. Laplanche, "Effects of Cr/Ni ratio on physical properties of Cr–Mn–Fe–Co–Ni high-entropy alloys," *Acta Mater.* **227**, 117693 (2022).
- ¹³ Z. Rao, P.-Y. Tung, R. Xie, Y. Wei, H. Zhang, A. Ferrari, T. Klaver, F. Körmann, P. T. Sukumar, A. Kwiatkowski da Silva, Y. Chen, Z. Li, D. Pong, J. Neugebauer, O. Gutfleisch, S. Bauer, and D. Raabe, "Machine learning-enabled high-entropy alloy discovery," *Science* **378**, 78–85 (2022).
- ¹⁴ A. Abu-Odeh, E. Galvan, T. Kirk, H. Mao, Q. Chen, P. Mason, R. Malak, and R. Arróyave, "Efficient exploration of the high entropy alloy composition-phase space," *Acta Mater.* **152**, 41–57 (2018).
- ¹⁵ C. Yang, C. Ren, Y. Jia, G. Wang, M. Li, and W. Lu, "A machine learning-based alloy design system to facilitate the rational design of high entropy alloys with enhanced hardness," *Acta Mater.* **222**, 117431 (2022).
- ¹⁶ Z. Pei, J. Yin, P. K. Liaw, and D. Raabe, "Toward the design of ultrahigh-entropy alloys via mining six million texts," *Nat. Commun.* **14**, 54 (2023).
- ¹⁷ S. Li, S. Li, D. Liu, R. Zou, and Z. Yang, "Hardness prediction of high entropy alloys with machine learning and material descriptors selection by improved genetic algorithm," *Comput. Mater. Sci.* **205**, 111185 (2022).
- ¹⁸ X. Liu, J. Zhang, and Z. Pei, "Machine learning for high-entropy alloys: Progress, challenges and opportunities," *Prog. Mater. Sci.* **131**, 101018 (2023).
- ¹⁹ J. Zhang, X. Liu, S. Bi, J. Yin, G. Zhang, and M. Eisenbach, "Robust data-driven approach for predicting the configurational energy of high entropy alloys," *Mater. Des.* **185**, 108247 (2020).
- ²⁰ C. Tandoc, Y.-J. Hu, L. Qi, and P. K. Liaw, "Mining of lattice distortion, strength, and intrinsic ductility of refractory high entropy alloys," *npj Comput. Mater.* **9**, 53 (2023).
- ²¹ N. Linton and D. S. Aidhy, "A machine learning framework for elastic constants predictions in multi-principal element alloys," *APL Mach. Learn.* **1**, 016109 (2023).
- ²² R. Li, L. Xie, W. Y. Wang, P. K. Liaw, and Y. Zhang, "High-throughput calculations for high-entropy alloys: A brief review," *Front. Mater.* **7**, 290 (2020).
- ²³ U. Bhandari, C. Zhang, C. Zeng, S. Guo, and S. Yang, "Computational and experimental investigation of refractory high entropy alloy Mo₁₅Nb₂₀Re₁₅Ta₃₀W₂₀," *J. Mater. Res. Technol.* **9**, 8929–8936 (2020).
- ²⁴ L. Zhang, K. Qian, B. W. Schuller, and Y. Shibuta, "Prediction on mechanical properties of non-equiatomic high-entropy alloy by atomistic simulation and machine learning," *Metals* **11**, 922 (2021).
- ²⁵ Y. Lederer, C. Toher, K. S. Vecchio, and S. Curtarolo, "The search for high entropy alloys: A high-throughput *ab initio* approach," *Acta Mater.* **159**, 364–383 (2018).
- ²⁶ Z. Ren, Z. Ren, Z. Zhang, T. Buonassisi, and J. Li, "Autonomous experiments using active learning and AI," *Nat. Rev. Mater.* **8**, 563–564 (2023).
- ²⁷ D. Khatamsaz, B. Vela, P. Singh, D. D. Johnson, D. Allaire, and R. Arróyave, "Multi-objective materials Bayesian optimization with active learning of design constraints: Design of ductile refractory multi-principal-element alloys," *Acta Mater.* **236**, 118133 (2022).
- ²⁸ D. Khatamsaz, B. Vela, P. Singh, D. D. Johnson, D. Allaire, and R. Arróyave, "Bayesian optimization with active learning of design constraints using an entropy-based approach," *npj Comput. Mater.* **9**, 49 (2023).
- ²⁹ T. Mohanty, K. Chandran, and T. D. Sparks, "Machine learning guided optimal composition selection of niobium alloys for high temperature applications," *APL Mach. Learn.* **1**, 036102 (2023).
- ³⁰ A. E. Siemenn, Z. Ren, Q. Li, and T. Buonassisi, "Fast Bayesian optimization of Needle-in-a-Haystack problems using zooming memory-based initialization (ZoMBI)," *npj Comput. Mater.* **9**, 79 (2023).
- ³¹ G. Bracq, M. Laurent-Brocq, L. Perrière, R. Pirès, J.-M. Joubert, and I. Guillot, "The fcc solid solution stability in the Co–Cr–Fe–Mn–Ni multi-component system," *Acta Mater.* **128**, 327–336 (2017).
- ³² M. G. Poletti and L. Battezzati, "Electronic and thermodynamic criteria for the occurrence of high entropy alloys in metallic systems," *Acta Mater.* **75**, 297–306 (2014).
- ³³ J.-C. Crivello, J.-M. Joubert, and N. Sokolovska, "Supervised deep learning prediction of the formation enthalpy of complex phases using a DFT database: The σ -phase as an example," *Comput. Mater. Sci.* **201**, 110864 (2022).
- ³⁴ N. Saunders and A. P. Miodownik, *CALPHAD (Calculation of Phase Diagrams): A Comprehensive Guide* (Elsevier, 1998).
- ³⁵ A. Gelman, J. B. Carlin, H. S. Stern, D. B. Dunson, A. Vehtari, and D. B. Rubin, *Bayesian Data Analysis* (CRC Press, 2013).
- ³⁶ D. Eriksson, M. Pearce, J. Gardner, R. D. Turner, and M. Poloczek, "Scalable global optimization via local Bayesian optimization," *Adv. Neural Inf. Proc. Syst.* **32**, 5496–5507 (2019).
- ³⁷ Q. Liang, A. E. Gongora, Z. Ren, A. Tihihonen, Z. Liu, S. Sun, J. R. Deneault, D. Bash, F. Mekki-Berrada, S. A. Khan *et al.*, "Benchmarking the performance of Bayesian optimization across multiple experimental materials science domains," *npj Comput. Mater.* **7**, 188 (2021).
- ³⁸ A. Banerjee, D. B. Dunson, and S. T. Tokdar, "Efficient Gaussian process regression for large datasets," *Biometrika* **100**, 75–89 (2013).
- ³⁹ F. Pedregosa, G. Varoquaux, A. Gramfort, V. Michel, B. Thirion, O. Grisel, M. Blondel, P. Prettenhofer, R. Weiss, V. Dubourg, J. Vanderplas, A. Passos, D. Cournapeau, M. Brucher, M. Perrot, and E. Duchesnay, "Scikit-learn: Machine learning in Python," *J. Mach. Learn. Res.* **12**, 2825–2830 (2011).
- ⁴⁰ I. Y. Miranda-Valdez, L. Viitanen, J. Mac Intyre, A. Puisto, J. Koivisto, and M. Alava, "Predicting effect of fibers on thermal gelation of methylcellulose using Bayesian optimization," *Carbohydr. Polym.* **298**, 119921 (2022).
- ⁴¹ K. Morita, Y. Nishikawa, and M. Ohzeki, "Random postprocessing for combinatorial Bayesian optimization," *J. Phys. Soc. Jpn.* **92**, 123801 (2023).
- ⁴² R. Otis and Z.-K. Liu, "pypcalphad: CALPHAD-based computational thermodynamics in Python," *J. Open Res. Software* **5**, 1 (2017).
- ⁴³ C. W. Bale, E. Bêlisle, P. Chartrand, S. Decterov, G. Eriksson, A. E. Gheribi, K. Hack, I.-H. Jung, Y.-B. Kang, J. Melançon, A. Pelton, S. Petersen, C. Robelin, J. Sangster, P. Spencer, and M.-A. Van Ende, "Reprint of: FactSage thermochemical software and databases, 2010–2016," *Calphad* **55**, 1–19 (2016).
- ⁴⁴ A. P. Thompson, H. M. Aktulga, R. Berger, D. S. Bolintineanu, W. M. Brown, P. S. Crozier, P. J. in't Veld, A. Kohlmeyer, S. G. Moore, T. D. Nguyen, R. Shan,

- M. J. Stevens, J. Tranchida, C. Trott, S. J. Plimpton, and S. J. Plimpton, "LAMMPS—A flexible simulation tool for particle-based materials modeling at the atomic, meso, and continuum scales," *Comput. Phys. Commun.* **271**, 108171 (2022).
- ⁴⁵W.-M. Choi, Y. H. Jo, S. S. Sohn, S. Lee, and B.-J. Lee, "Understanding the physical metallurgy of the CoCrFeMnNi high-entropy alloy: An atomistic simulation study," *npj Comput. Mater.* **4**, 1 (2018).
- ⁴⁶R. Alvarez-Donado, S. Bonfanti, and M. Alava, "Simulated multi-component CuZr(Al) metallic glasses akin to experiments," arXiv:2309.05806 (2023).
- ⁴⁷Z. Wang, L. Li, Z. Chen, K. Yuge, K. Kishida, H. Inui, and M. Heilmaier, "A new route to achieve high strength and high ductility compositions in Cr–Co–Ni-based medium-entropy alloys: A predictive model connecting theoretical calculations and experimental measurements," *J. Alloys Compd.* **959**, 170555 (2023).
- ⁴⁸Z. Zhang, M. Mao, J. Wang, B. Gludovatz, Z. Zhang, S. X. Mao, E. P. George, Q. Yu, and R. O. Ritchie, "Nanoscale origins of the damage tolerance of the high-entropy alloy CrMnFeCoNi," *Nat. Commun.* **6**, 10143 (2015).
- ⁴⁹B. Gludovatz, A. Hohenwarter, K. V. Thurston, H. Bei, Z. Wu, E. P. George, and R. O. Ritchie, "Exceptional damage-tolerance of a medium-entropy alloy CrCoNi at cryogenic temperatures," *Nat. Commun.* **7**, 10602 (2016).
- ⁵⁰W. Xia, X. Zhao, L. Yue, and Z. Zhang, "A review of composition evolution in Ni-based single crystal superalloys," *J. Mater. Sci. Technol.* **44**, 76–95 (2020).
- ⁵¹R. Garnett, *Bayesian Optimization* (Cambridge University Press, 2023).
- ⁵²R. Hickman, M. Aldeghi, and A. Aspuru-Guzik, "Anubis: Bayesian optimization with unknown feasibility constraints for scientific experimentation," chemRxiv (2023) <https://doi.org/10.26434/chemrxiv-2023-s5qnw>.
- ⁵³R. Arróyave, D. Khatamsaz, B. Vela, R. Couperthwaite, A. Molkeri, P. Singh, D. D. Johnson, X. Qian, A. Srivastava, and D. Allaire, "A perspective on Bayesian methods applied to materials discovery and design," *MRS Commun.* **12**, 1037 (2022).
- ⁵⁴G. Chen, J. Qiao, Z. Jiao, D. Zhao, T. Zhang, S. Ma, and Z. Wang, "Strength-ductility synergy of Al_{0.1}CoCrFeNi high-entropy alloys with gradient hierarchical structures," *Scr. Mater.* **167**, 95–100 (2019).
- ⁵⁵P. Shi, W. Ren, T. Zheng, Z. Ren, X. Hou, J. Peng, P. Hu, Y. Gao, Y. Zhong, and P. K. Liaw, "Enhanced strength–ductility synergy in ultrafine-grained eutectic high-entropy alloys by inheriting microstructural lamellae," *Nat. Commun.* **10**, 489 (2019).
- ⁵⁶J. Ren, Y. Zhang, D. Zhao, Y. Chen, S. Guan, Y. Liu, L. Liu, S. Peng, F. Kong, J. D. Poplawsky, G. Gao, T. Voisin, K. An, Y. M. Wang, K. Y. Xie, T. Zhu, and W. Chen, "Strong yet ductile nanolamellar high-entropy alloys by additive manufacturing," *Nature* **608**, 62–68 (2022).
- ⁵⁷O. K. Orhan, M. Isiet, L. Caparini, and M. Ponga, "Exploring the compositional space of high-entropy alloys for cost-effective high-temperature applications," *Front. Mater.* **8**, 816610 (2022).
- ⁵⁸Y. Wu, F. Zhang, X. Yuan, H. Huang, X. Wen, Y. Wang, M. Zhang, H. Wu, X. Liu, H. Wang, S. Jiang, and Z. Lu, "Short-range ordering and its effects on mechanical properties of high-entropy alloys," *J. Mater. Sci. Technol.* **62**, 214–220 (2021).
- ⁵⁹S. Bonfanti, R. Guerra, R. Alvarez-Donado, P. Sobkowicz, S. Zapperi, and M. Alava, "Quasilocalized modes in crystalline and partially crystalline high-entropy alloys," *Phys. Rev. Res.* **6**, 013146 (2024).
- ⁶⁰Z. Fan, L. Li, Z. Chen, M. Asakura, C. Zhang, Z. Yang, H. Inui, and E. P. George, "Temperature-dependent yield stress of single crystals of non-equiatomic Cr–Mn–Fe–Co–Ni high-entropy alloys in the temperature range 10–1173 K," *Acta Mater.* **246**, 118712 (2023).
- ⁶¹C. A. Becker, F. Tavazza, Z. T. Trautt, and R. A. Buarque de Macedo, "Considerations for choosing and using force fields and interatomic potentials in materials science and engineering," *Curr. Opin. Solid State Mater. Sci.* **17**, 277–283 (2013).
- ⁶²L. M. Hale, Z. T. Trautt, and C. A. Becker, "Evaluating variability with atomistic simulations: The effect of potential and calculation methodology on the modeling of lattice and elastic constants," *Modell. Simul. Mater. Sci. Eng.* **26**, 055003 (2018).
- ⁶³J. Byggmästar, K. Nordlund, and F. Djurabekova, "Modeling refractory high-entropy alloys with efficient machine-learned interatomic potentials: Defects and segregation," *Phys. Rev. B* **104**, 104101 (2021).
- ⁶⁴D. B. Miracle, J. D. Miller, O. N. Senkov, C. Woodward, M. D. Uchic, and J. Tiley, "Exploration and development of high entropy alloys for structural applications," *Entropy* **16**, 494–525 (2014).
- ⁶⁵Y. Zhang, Y. J. Zhou, J. P. Lin, G. L. Chen, and P. K. Liaw, "Solid-solution phase formation rules for multi-component alloys," *Adv. Eng. Mater.* **10**, 534–538 (2008).
- ⁶⁶N. L. Okamoto, K. Yuge, K. Tanaka, H. Inui, and E. P. George, "Atomic displacement in the CrMnFeCoNi high-entropy alloy—A scaling factor to predict solid solution strengthening," *AIP Adv.* **6**, 125008 (2016).